Journal of Energy Chemistry 117 (2026) 880–892

Contents lists available at ScienceDirect

Journal of Energy Chemistry

journal homepage: www.elsevier.com/locate/jechem

http://www.journals.elsevier.com/journal-of-energy-chemistry/

Above 10% efficiency flexible inkjet-printed kesterite solar cells

Berenice Elena Gaia Colombo [a,1], Alex Sangiorgi [b,1], Giorgio Tseberlidis [a,b,*], Carla Gobbo [a], Fabio Butrichi [a], Vanira Trifiletti [a], Maurizio Acciarri [a], Alessandra Sanson [b], Simona Binetti [a]

[a] Department of Materials Science and Solar Energy Research Center (MIB-SOLAR), University of Milano-Bicocca, Milano 20125, Italy
[b] CNR-ISSMC Istituto di Scienza, Tecnologia e Sostenibilità per lo sviluppo dei Materiali Ceramici, Faenza RA 48018, Italy

ARTICLE INFO

Article history:
Received 27 November 2025
Revised 11 February 2026
Accepted 4 March 2026
Available online 17 March 2026

Keywords:
Kesterite
Flexible
Solar cells
Inkjet printing
Integrated photovoltaics

ABSTRACT

$Cu_2ZnSn(S,Se)_4$ (CZTSSe or kesterite) is an emerging inorganic light absorber with a bandgap of 1.0–1.5 eV, ideal for efficient solar spectrum harvesting. This material can be grown on both rigid and flexible substrates, standing as one of the most promising candidates for Integrated Photovoltaics. Solution-based methods are currently the best choice for CZTSSe synthesis, relying on the deposition of multiple layers. The most widely used techniques are blade coating, spray pyrolysis, dip coating, and spin coating, with the latter achieving the highest efficiencies. However, this technology's small-area limitations and large precursor waste still hinder the kesterite solar cells' scalability. In contrast, drop-on-demand inkjet printing is a promising and industrially appealing solution-based technique suitable for processing large areas. To date, it has been tested in a few cases, yielding encouraging results with rigid solar devices; however, it has never been used to fabricate flexible CZTSSe solar cells. In this work, we report on the first-time realization of inkjet-printed flexible kesterite solar cells. The resulting devices exhibit an efficiency enhancement over our spin-coated references, driven by improved film crystallinity, reduced shunting, and enhanced fill factor. The inkjet-printed flexible champion device achieved an efficiency of 10.4%, outperforming our spin-coated reference counterpart. Structural, morphological, and optoelectronic analyses confirm the superior quality of the inkjet-deposited absorber. This scalable, solution-based approach establishes a pathway for the roll-to-roll fabrication of earth-abundant, lightweight kesterite photovoltaics for next-generation, integrated, and flexible photovoltaic applications, a key factor for the advancement of kesterite materials in the photovoltaic sector.

1. Introduction

Among the emerging thin-film photovoltaic (PV) technologies, we find kesterite-based PV absorbers, mainly represented by solar cells exploiting the sulfo-selenide compound $Cu_2ZnSn(S,Se)_4$ (CZTSSe) [1–4]. They are p-type semiconductors with a high absorption coefficient (>10^4 cm^{-1}) and a direct energy gap in the 1.0–1.5 eV range (according to the sulfur-selenium ratio). Due to their apparent structural similarity, kesterites are frequently associated with the already commercialized $CuInGaSe_2$ (CIGS) [5], where the expensive In and Ga are replaced with Earth-abundant Zn and Sn. In the "Terawatt Era" scenario, PV will be of fundamental importance, adapting to many applications that require lightweight technologies such as integrated PV [6,7]. Considering the production costs of CIGS and the toxicity associated with the use of Cd in CdTe [8], the research for a sustainable alternative to inorganic thin-film PV technology has prompted the scientific community to investigate kesterites as a viable low-cost alternative. Katagiri reported the first kesterite solar cell in 1997 with an efficiency (η) of 0.66% [9], followed by an efficiency increase until the current record of η = 15.85% in 2025 [10]. Although vacuum-based methods have traditionally been the preferred choice for CIGS deposition, it has been demonstrated that CZTSSe can be more effectively grown through solution-based methods [2,3]. Among them, we find spin-coating, blade-coating, spray pyrolysis, and dip-coating, with spin-coating yielding the current record efficiencies [10–27]. However, the small-area limitations of this technology, combined with the waste of large volumes of precursor solution, still hinder the kesterite solar cells' broad applicability and scalability [28]. Inkjet printing is a promising, fully automated solution-based technique [29], extremely adaptable to large areas and to roll-to-roll process, with almost-zero materials waste and

* Corresponding author.
E-mail address: giorgio.tseberlidis@unimib.it (G. Tseberlidis).
[1] These authors contributed equally to this work.

https://doi.org/10.1016/j.jechem.2026.03.011

a remarkable industrial appeal, which has been tested only in a few cases, recording promising results and leading to good quality solar devices, but only on rigid substrates based on glass [23,30–32]. Back in 2015, Lin and co-workers reported the first study on glass-based inkjet-printed CZTSSe solar cells, with η = 6.4% starting from a DMSO-based ink [30]. Later, η = 9.2% efficient CZTSSe solar cells have been reported starting from a DMSO/DMF-based precursor [31]. The reduced stability of DMSO- and DMF-based inks, due to their rheological properties and the poor wettability of the Mo layer conventionally used as back contact in CZTSSe solar cells, recently prompted the scientific community to shift the solvent choice toward 2-methoxyethanol (MOE) in order to obtain more stable precursor inks. These novel inks have been successfully employed both through spin-coating and inkjet printing on glass-based rigid substrates, leading to very promising results [23,32,33]. However, despite the importance of adapting thin-film PV to integrated emerging applications needing lightweight technologies, to date, no CZTSSe solar cell inkjet-printed on flexible substrates has been reported. In this study, a stable and properly engineered MOE-based precursor ink is used to fabricate the first examples of flexible CZTSSe solar devices through inkjet printing, relying on flexible and lightweight Mo foils. The resulting devices not only equaled the efficiency of our corresponding spin-coated counterparts (η_{spin} = 9.6%) but also improved the overall cell parameters (η_{inkjet} = 10.4%), relying on a more homogenous, compact, and crystalline material, leading to better series and shunt resistance values (R_S and R_{SH}) and consequently to a higher fill factor (*FF*). Moreover, our inkjet-printed flexible solar cells recorded encouraging results during stress tests, retaining 90% of their starting PV parameters over 500 bending cycles, in contrast to the <65% PV retention by our spin-coated reference samples.

2. Experimental

2.1. Solution preparation

First, Thiourea (TU, 99%, Thermo Scientific), CuCl (99%, Thermo Scientific), and AgCl (99.9% Thermo Scientific) were mixed in a vial with 2-Methoxyethanol (MOE, 99.3+%, Thermo Scientific), to obtain the TU-Cu-Ag solution. Then, $Zn(CH_3CO_2)_2{\cdot}2H_2O$ (99.99%, Sigma-Aldrich) and $SnCl_4{\cdot}5H_2O$ (98+%, Thermo Scientific) were dissolved in a second vial with MOE to make the Sn-Zn solution. After complete dissolution under stirring, the two solutions were mixed. Finally, $LiClO_4$ (95.0%, Thermo Scientific) was dissolved in the precursor solution. Before the deposition, the precursor solution was filtered with a 0.2 μm PTFE Hydrophilic filter (Thermo Scientific). The precursor solutions' concentrations are reported in Table 1.

2.2. Substrate preparation

Commercially available Mo-foils (purity ≥ 99.99%, Matyasigo, China) with a thickness of 0.1 mm were cut into 2 cm × 2 cm samples and then pressed with the aid of a hydraulic press by using 15 tons at room temperature (RT) for 3 min. The so-obtained flat samples were cleaned with a Mucasol Universal Detergent (Thermo Scientific) solution in water, ultrasonically washed in deionized (DI) water for ten minutes, and finally dried under N_2 flow. As the final step, the Mo-foil samples were annealed at 450 °C for 10 min in air on a ceramic hot plate to thermally produce a golden-appearing MoO_x layer on their surface, which can enhance the substrate wettability, act as a barrier during the CZTSSe growth, and prevent back-contact degradation [22].

Table 1
Concentrations of precursor solutions.

Reagent	SOL-A	SOL-B
CuCl	0.465 M	0.581 M
AgCl	0.0516 M	0.0645 M
$Zn(CH_3CO_2)_2{\cdot}2H_2O$	0.364 M	0.455 M
$SnCl_4{\cdot}5H_2O$	0.331 M	0.414 M
$LiClO_4$	0.0113 M	0.0141 M
Thiourea	2.21 M	2.76 M

2.3. Thin film deposition with spin-coating

The filtered precursor solution was spin-coated using SCS G3P-8 Spincoat Speciality Coating Systems (Cookson Electronics Company) at 3000 r min^{-1} for 30 s onto the previously described Mo-Foil/MoO_x substrates. The so-obtained films were dried on a hot plate at 280 °C for 2 min and then rapidly cooled to RT. This deposition-drying cycle was repeated 8 to 9 times to achieve the desired thickness.

2.4. Thin film deposition with inkjet printing

The precursor solution, after filtration, was loaded into the 5 mL ink tank of a piezo-driven printing head, MD-K-140 (Microdrop Technologies GmbH, Germany), for drop-on-demand (DoD) inkjet printing. This device, with a nozzle diameter of 70 μm and the possibility to print fluids with viscosity in the range of 0.4–100 mPa s, is installed in a stand-alone working station (XCEL, AUREL Automation, Italy) that allows both to control several printing parameters, such as desired patterns and printing speed, and to optimize single droplets through a drop watcher system. Regarding optimization, in this type of DoD inkjet printing, drops are ejected due to the propagation of a pressure pulse in the fluid-filled chamber near the printing nozzle. This phenomenon is primarily determined by the deformation of the piezoelectric actuator, which is obtained by varying the applied voltage magnitude, the actuating pulse duration, and its frequency. With this precursor solution, the best results in terms of drop shape and dimensions were obtained with an applied voltage of 180 V and a pulse duration of 38 μs, at a frequency of 1036 Hz. Finally, to keep the ink meniscus stuck to the printing nozzle, the holding pressure in the ink tank was adjusted to −10 mbar. Snake-like patterns, with a curvature radius of 100 μm and 150 μm, were reliably printed onto Mo-Foil/MoO_x substrates at 30 mm s^{-1} as printing speed. The as-produced films were then dried and cooled following the same protocol as the spin-coated ones. The suitable film thickness was achieved by repeating this deposition-drying cycle 7 to 8 times.

2.5. Thin film annealing and CZTSSe phase formation

The so-obtained samples were put into a quartz box in the presence of Se pellets (Umicore, 99.995%) and annealed in an Ar-flowed reactor (0.1 L min^{-1}), with the aid of a tubular furnace, starting from RT to 580 °C with a rate of 18.7 °C min^{-1}, followed by an isotherm at 580 °C for 20 min. Finally, the Ar-flowed quartz reactor was allowed to cool down to RT with an Ar flow of 0.5 L min^{-1}. The so-obtained absorbers' final thickness results in 1.5–1.6 μm.

2.6. PV device preparation

All the samples were finalized for PV devices using the following procedure: a CdS buffer layer (40 nm) was deposited by chemical bath deposition in an aqueous solution of NH_3 (Fisher Chemical, 35% for HPLC) and NH_4Cl (AnalaR NORMAPUR® ACS VWR Chemicals, 99.8–100.5%), using $Cd(CH_3COO)_2{\cdot}2H_2O$ (Thermo Scientific, 98%) and TU at 75 °C for ten minutes. A thin i-ZnO layer (50 nm) was deposited by magnetron sputtering, and Al-doped ZnO (AZO) was chosen as the top contact and deposited by DC

pulsed (2 kHz) magnetron sputtering with a thickness of 300 nm. The devices were completed by evaporating 350 nm of Al grid, followed by thermal treatment in air at 260 °C for 10 min. Finally, solar cells with an area of 0.16 cm^2 were singularly isolated through manual scribing and singularly contacted and measured with no need for any masking area. Some of the devices (as described in the Results and Discussion section) have been further processed by evaporating MgF_2 (100 nm) as an anti-reflective coating (ARC) to diminish the residual reflectance mainly caused by the i-ZnO and AZO top layers.

2.7. Characterization

The dynamic viscosity analysis of the filtered precursor solution was performed by a Bohlin C-VOR rheometer (Malvern Instruments Ltd., UK) equipped with parallel plates with a diameter of 60 mm and a gap of 0.75 mm. The test was conducted at 25 °C in controlled stress mode, with a shear range of 0.010–10000 Pa and a sweep time of 180 s. At ambient conditions, the solution surface tension was determined using a drop shape analyser, DSA30 Tensiometer (Krüss, Germany), in pendant drop configuration. Finally, its density was calculated by weighing 5 mL of solution on a microbalance. These physical parameters, used to optimize liquid jetting and its deposition, are tied to the Ohnesorge number or, more frequently, its inverse. The so-called Z parameter that defines the optimal printability of fluids can be calculated following Eq. (1).

$$Z = \frac{1}{Oh} = \frac{Re}{\sqrt{We}} = \frac{\sqrt{\sigma \rho a}}{\mu} \quad (1)$$

where Oh is the Ohnesorge number, while Re and We are the Reynolds and Weber numbers, respectively. Moreover, σ (mN m^{-1}), μ (mPa s), and ρ (g cm^{-3}) are the surface tension, viscosity, and density of the ink, while a (μm) is commonly assimilated to the nozzle diameter. In the inkjet printing field, the range of $1 < Z < 10$ is commonly considered optimal. The solution's capability to properly wet the desired substrate was evaluated through contact angle analysis, performed with the same DSA30 tensiometer working with the sessile drop method [34]. The thickness of the CZTSSe thin films was measured using a Veeco-Dektak 150 profilometer. The crystallographic data of the CZTSSe flexible devices were collected by X-ray diffraction (XRD) performed by a Rigaku Miniflex 600 apparatus (F.F tube 40 kV, 15 mA, DS/SS = 1.25°, RS = 0.3 mm, HyPix-400 MF 2D-HPAD). Raman spectra of all thin films were recorded by a Jasco Ventuno μ-Raman system, equipped with a Peltier-cooled charge-coupled device (operating temperature: −50 °C) by using a He-Ne laser (wavelength 632.8 nm, power density 6 kW cm^{-2}) as light source, to confirm the single-phase kesterite CZTSSe formation. Raman spectra have been calibrated before each measurement using a single crystal Si reference sample by imposing the position of the dominant Si peak at 520.65 cm^{-1}, and deconvolution was made utilizing OriginPro 2023. The solar cells were characterized using a 500 W xenon light source (ABET Technologies Sun 2000 class ABA Solar Simulator), calibrated to AM 1.5 (100 mW cm^{-2}) by a reference Si cell photodiode and an IR cut-off filter (KG-5, Schott) to reduce the mismatch between the simulated light and the AM 1.5 spectrum in the 350–750 nm range. The *J-V* curves were measured by applying an external bias to the device and recording the generated photocurrent with a Keithley model 2460 digital source meter. The measurement parameters were: range of measurement (from −300 to 700 mV); number of points (100); step (10 mV); sweep delay (10 ms); config delay (10 ms); sweep timeout (100 s). Scans forward and back have been recorded to check for eventual hysteresis. External quantum efficiency (EQE) measurements were recorded using a SpeQuest quantum efficiency system, as a function of excitation wavelength by using a monochromator (Omni 300 LOT ORIEL) with a single grating in Czerny-Turner optical design, in AC mode with a chopping frequency of 78 Hz. EQE measurements have been carried out using a circular spot of 0.1 cm^2 area which was partially shaded by the geometry of the Al contacts of the sample, thus able to provide only qualitative information. Planar SEM imaging was performed by using a Thermo Fisher Phenom G6 apparatus, equipped with a thermionic emission source (resolution < 6 nm at 15 kV using an Everhart-Thornley type detector for the secondary electron). Cross-section SEM imaging and EDS was performed by using a Gemini 500 Zeiss equipped with QUANTAX EDS 4000, EBSD, STEM. For the solar cell fitting and simulations, SCAPS-1D software, developed by the University of Gent, Department of Electronics and Information Systems (ELIS), has been used [35]. The program simulates thin-film heterojunction solar cells' DC and AC electrical characteristics. The model is based on solving the basic semiconductor equations (Poisson equation and the electron and hole continuity equations) having as the main functionality to solve the one-dimensional equations. The simulated illumination is set on the front contact with AM 1.5 global spectrum with a light power of one sun (100 mW cm^{-2}).

3. Results and discussion

First, in order to assure the applicability of the CZTSSe precursor solutions by inkjet printing (prepared as described in the previous section and reported in Table 1), their flow curve (shear rate vs. viscosity) was primarily acquired. The filtered solutions show a perfect Newtonian behavior in which the viscosity is constant regardless of the applied shear stress, and it is equal to 7.60 mPa s for SOL-A and 9.05 mPa s for SOL-B. Considering these values, suitable for the MD-K-140 print head, and the solutions density and surface tension of 1.11 g cm^{-3} and 41.04 mN m^{-1} for SOL-A and 1.60 g cm^{-3} and 34.74 mN m^{-1} for SOL-B, the resulting Z parameter was 7.43 for SOL-A and 5.86 for SOL-B. Both Z parameters fall within the optimal printability range; however, the value for SOL-B is located near the exact midpoint of it, where the droplet jet is expected to deliver the best performance in terms of directionality, droplet formation, and uniformity of shape and size. Concerning the entire deposition process, aiming to produce a homogeneous film without defects, another crucial aspect that must be evaluated is the fluid's ability to wet the substrate properly. Contact angle analyses were performed on the engineered Mo-foil substrates at room temperature to assess this capacity. The obtained results, equal to 12.5° ± 0.1° for SOL-A and 13.0° ± 1.5° for SOL-B, suggest an easy substrate wettability using both solutions, as confirmed by the fast drop spreading onto the small metal sheet during the inkjet printing process. This is the desired liquid-substrate interaction to produce homogeneous films over large areas. The desired snake-like patterns generated compact and homogeneously distributed films where the distance between single lines, directly dependent on the fixed curvature radius of 100 μm for SOL-A and 150 μm for SOL-B, allowed them to coalesce with almost no overlap, thus guaranteeing the minimal surface roughness.

After deposition and annealing of the CZTSSe thin-films, as described in Section 2.5, the structural and morphological properties of the absorbers were studied to ensure the high quality of the CZTSSe quaternary phase. Therefore, the thin films were analyzed via XRD. Good crystalline quality can be inferred by XRD analysis for both spin-coated and inkjet-printed samples, regardless of the precursor solution used. Fig. 1 depicts a typical XRD pattern of CZTSSe layers showing intense and sharp diffraction peaks related to the CZTSSe pure phase (DB card number 00-052-0868). No

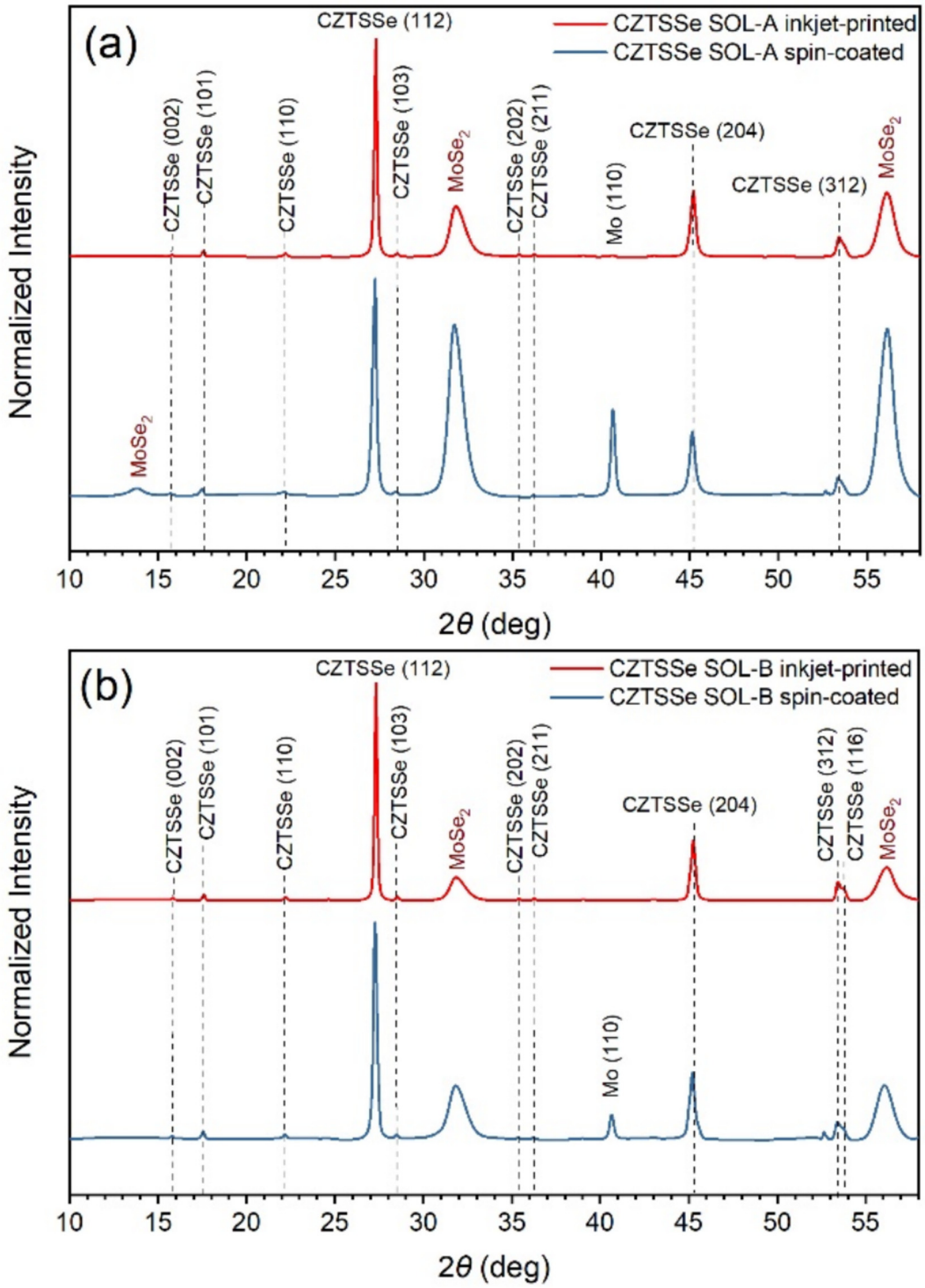

Fig. 1. (a) XRD pattern of spin-coated (blue) and inkjet-printed (red) CZTSSe thin-films produced with SOL-A; (b) XRD pattern of spin-coated (blue) and inkjet-printed (red) CZTSSe thin-films produced with SOL-B.

traces of crystalline secondary phases can be detected in none of the thin-films produced. The peak at 2θ values of 40.6° is attributed to Mo-foil used as the substrate [36,37]. Peaks at 2θ = 13.8°, 31.7°, and 56.1° can be associated with $MoSe_2$ formed at the interface between CZTSSe and Mo-foil substrate through annealing of the substrate as indicated in Section 2.5 [31,32]. The $MoSe_2$ growth was controlled by introducing a MoO_x barrier/sacrificial layer, which not only enhances the wettability of the substrate but also prevents the Mo foil degradation through excessive Se diffusion during the CZTSSe phase formation at high temperatures [22,38]. It is possible to notice how the normalized intensity of $MoSe_2$ peaks decreases when inkjet-printing is adopted as deposition method, especially when SOL-B is employed (Fig. 1). This can be ascribed to the formation of more compact layers, which hinder the Se diffusion through the back-contact interface during the oven-annealing step. By comparing the FWHM data of our

spin-coated samples with inkjet-printed ones, it is possible to infer a higher crystallinity of the latter regardless of the employed solution. In particular, when SOL-A is used (Fig. 1a), the FWHM value of the CZTSSe (112) main peak (2θ = 27.2° is 0.253 vs. 0.164, respectively, for spin-coated and inkjet-printed samples. On the other hand, the FWHM = 0.221 vs. 0.151 for spin-coated and inkjet-printed samples produced with SOL-B (Fig. 1b), thus demonstrating better crystallinity when SOL-B is employed together with inkjet deposition.

However, the crystal structure of CZTSSe is comparable to many of the possible binary and ternary phase compounds that can arise as by-products during the growth of kesterite thin films [1]. For this reason, XRD analysis is insufficient to determine the purity of the crystalline CZTSSe phase, necessitating the use of complementary characterization techniques, such as Raman spectroscopy. In the Raman spectra (Fig. 2), the presence of a pure CZTSSe phase, regardless of the precursor solution and deposition method used, is confirmed by the typical sharp and defined peaks around 248, 235, 196, and 172 cm^{-1}, as reported in the literature [39]. The characteristic peaks of detrimental secondary phases such as Cu_2SnSe_3, ZnSe, Cu_2Se, and SnSe are not detectable in any of the produced CZTSSe thin-films, as highlighted by the fitting and deconvolution

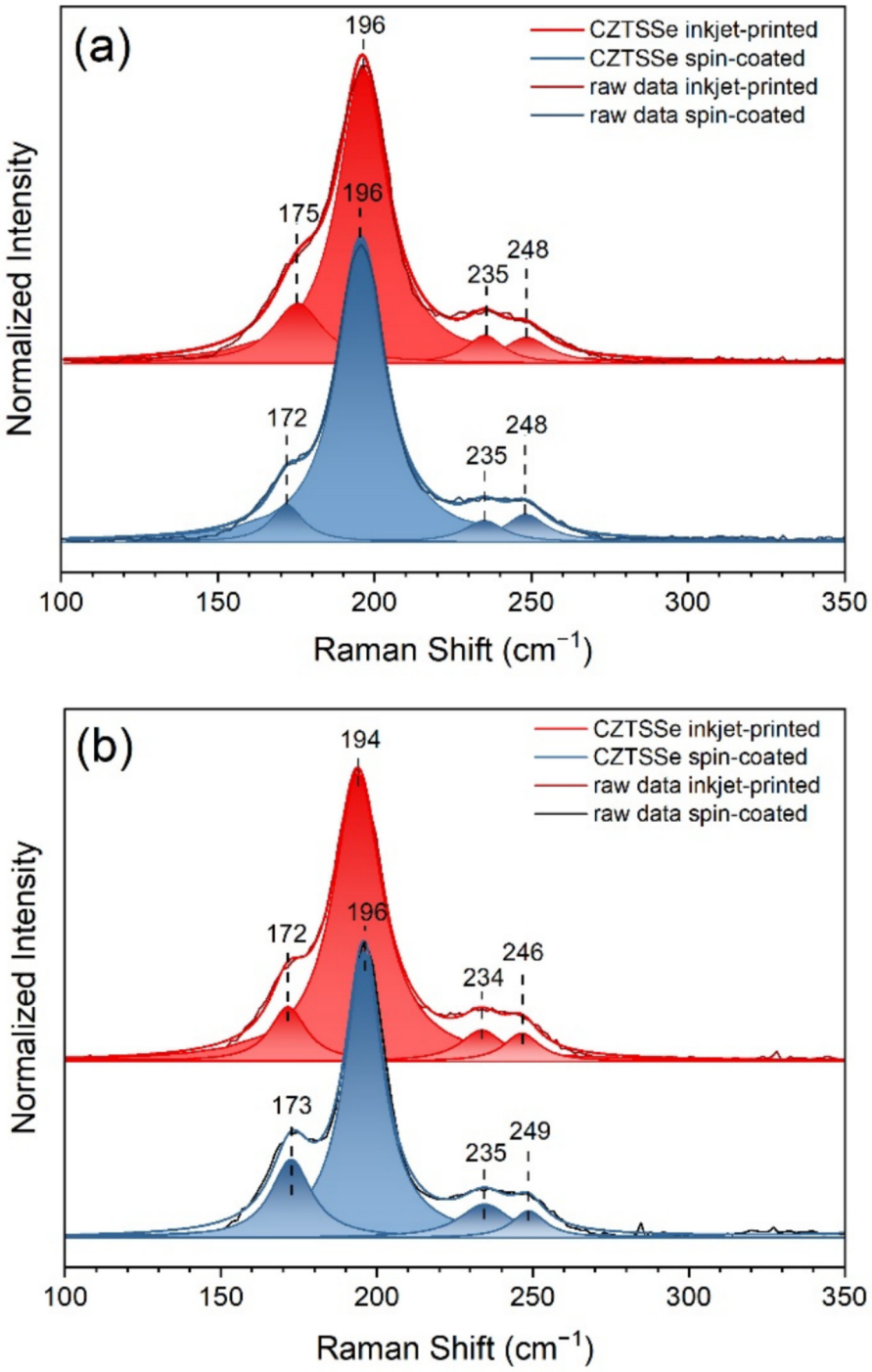

Fig. 2. (a) Raman spectra of spin-coated (blue; fitting R^2 = 0.9972) and inkjet-printed (red; fitting R^2 = 0.9946) CZTSSe thin-films produced with SOL-A; (b) Raman spectra of spin-coated (blue; fitting R^2 = 0.9945) and inkjet-printed (red; fitting R^2 = 0.9947) CZTSSe thin-films produced with SOL-B.

of the spectra. This confirms that the CZTSSe phase is properly formed, thanks to the optimal composition (in terms of metal ratio) of both the precursor solutions [33].

Upon completion of the devices with the architecture described in Section 2.6, by testing the resulting flexible solar cells, both SOL-A and SOL-B spin-coated and inkjet-printed, the effective charge carrier photogeneration and collection are confirmed by the *J-V* characteristics summarized in the box plots reported in Fig. 3. In the first instance, SOL-A led to inkjet-printed devices with slightly better parameters if compared to their spin-coated counterparts. The higher value of η_{max} = 6.4% is, however, counterbalanced by a similar mean value between spin-coated and inkjet-printed devices (η_{mean} = 4.8% vs. 4.9%), indicating a worse statistical distribution in the latter. These results can be ascribed to the non-optimal concentration of SOL-A, which cannot always guarantee a uniform and low-roughness surface of the CZTSSe absorber due to the possible formation of voids and cavities. On the other hand, by employing SOL-B, not only do the overall PV parameters increase for both spin-coated and inkjet-printed devices, but it also considerably narrows their statistical distribution by relying on a more compact and homogenous CZTSSe surface. Therefore, the mean efficiency for SOL-B spin-coated solar cells corresponds to $\eta_{mean\ spin}$ = 8.0% versus $\eta_{mean\ inkjet}$ = 8.8% for SOL-B inkjet-printed devices, with $\eta_{max\ spin}$ = 9.2% and $\eta_{max\ inkjet}$ = 9.7%. These data also show a better statistical distribution for the inkjet-printed devices, mainly ascribed to a considerable improvement in J_{SC} and *FF* values. In fact, both parameters can be related to the better-printable parameters of the SOL-B precursor solution during the inkjet deposition, which guaranteed a uniform and compact CZTSSe surface.

Prompted by these promising results and aware of the residual reflectance usually brought by the top transparent conductive oxide (TCO) layers (namely i-ZnO and AZO), the champion flexible SOL-B solar devices have been further processed by depositing 100 nm of MgF_2 as ARC, as described in the experimental section (Section 2.6). MgF_2 is conventionally employed as ARC in CZTSSe solar cells, and its beneficial impact has been repeatedly reported in the literature [10]. As a consequence, the updated box plots of all cells' parameters for ARC spin-coated and inkjet-printed flexible SOL-B devices describe a better light harvesting with enhanced efficiencies (Fig. 4). In particular, the mean efficiency of spin-coated SOL-B cells rises from $\eta_{mean\ spin}$ = 8.5% to 8.8%, with $\eta_{max\ spin}$ = 9.6%. As for the inkjet-printed SOL-B devices, the mean efficiency increases from $\eta_{mean\ inkjet}$ = 8.9% to 9.2%, with $\eta_{max\ inkjet}$ = 10.4%, which, to the best of our knowledge, is the first example (and therefore the record) for a flexible, but also inkjet-printed, CZTSSe solar cell. The ARC spin-coated devices show a fair mean value of J_{SC} (37.1 mA cm^{-2}), which is, however, surpassed by J_{SC} = 39.1 mA cm^{-2} recorded for the ARC inkjet-printed solar cells. Despite the evident improvement in η% mean values for both categories of ARC devices, the spin-coated ones exhibit a slight decrease in $FF_{mean\ spin}$ = 54.3%, compared to the improved $FF_{mean\ inkjet}$ = 60.1% of the ARC inkjet-printed cells. The

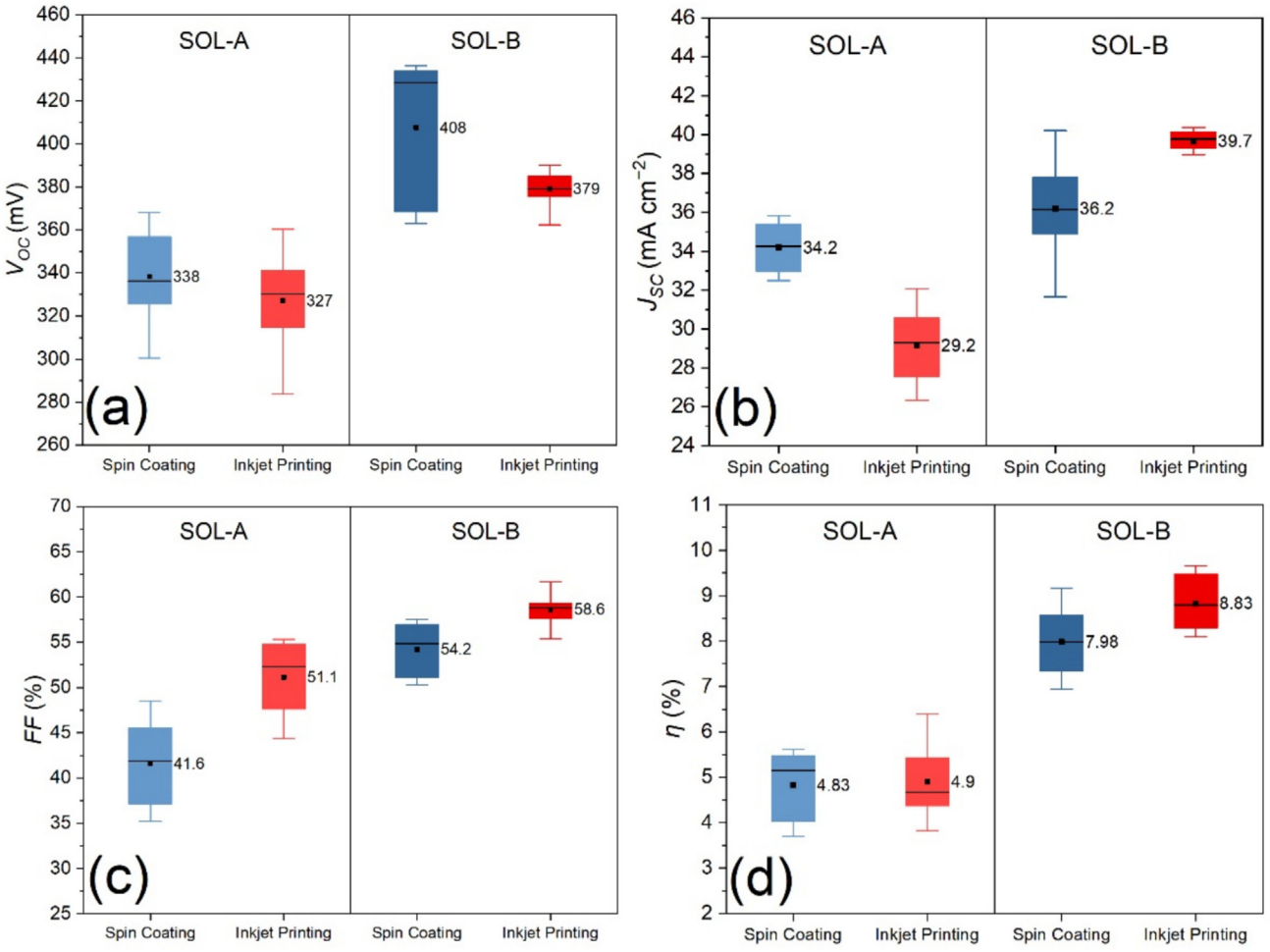

Fig. 3. Box Plots of the solar cell parameters V_{OC} (a), J_{SC} (b), *FF* (c), and η (d), for SOL-A and SOL-B spin-coated (blue) and inkjet-printed (red) devices (with their statistical distribution, corresponding mean value (black square) and median (black line) in the inset of each box).

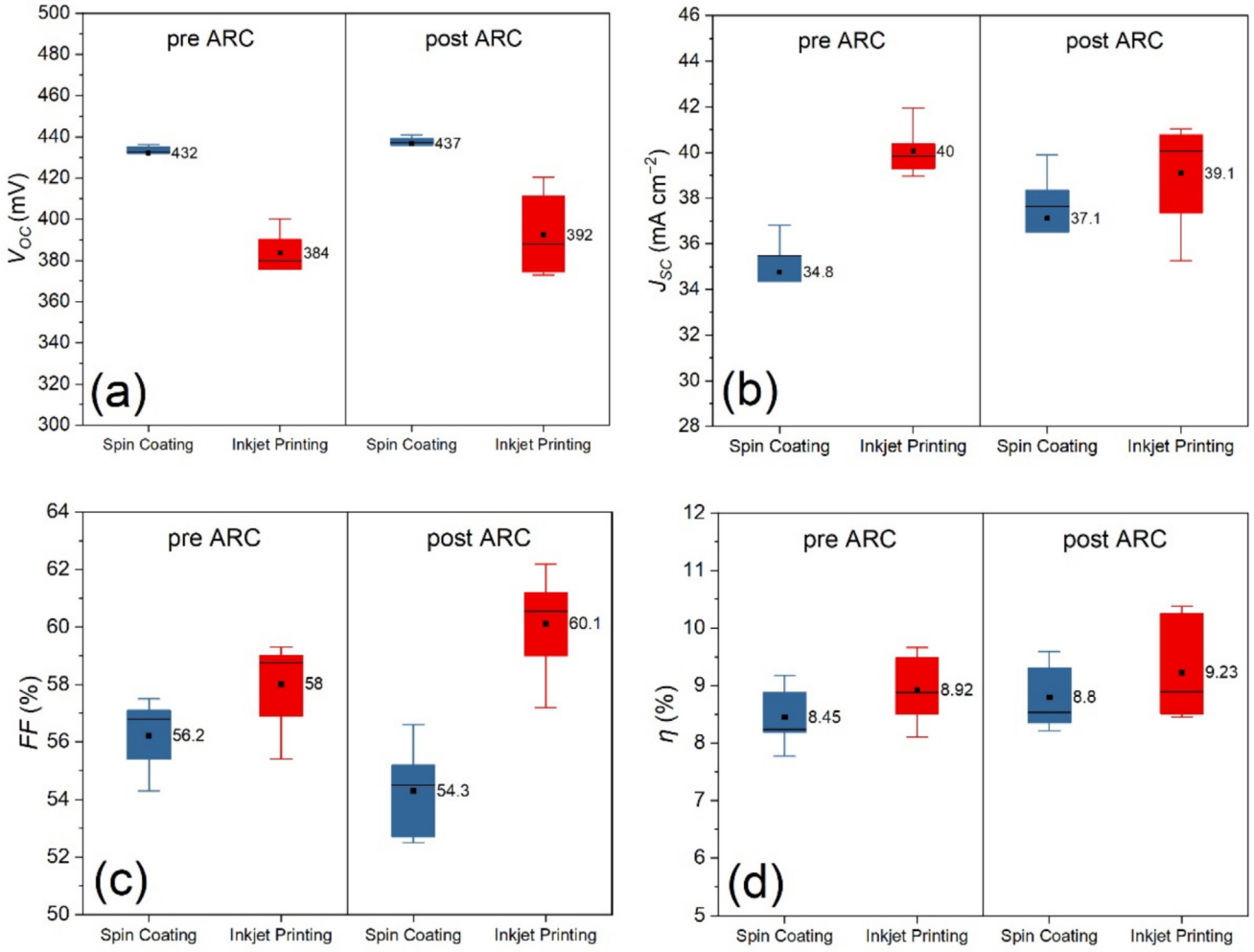

Fig. 4. Box Plots of the pre-ARC and post-ARC solar cell parameters V_{OC} (a), J_{SC} (b), *FF* (c), and η (d), for SOL-B spin-coated (blue) and inkjet-printed (red) devices (with their statistical distribution, corresponding mean value (black square) and median (black line) in the inset of each box).

corresponding *J-V* curves (pre- and post-ARC) for both the SOL-B spin-coated and inkjet-printed ARC champion devices are reported in Fig. 5 together with their complete PV parameters reported in Table 2.

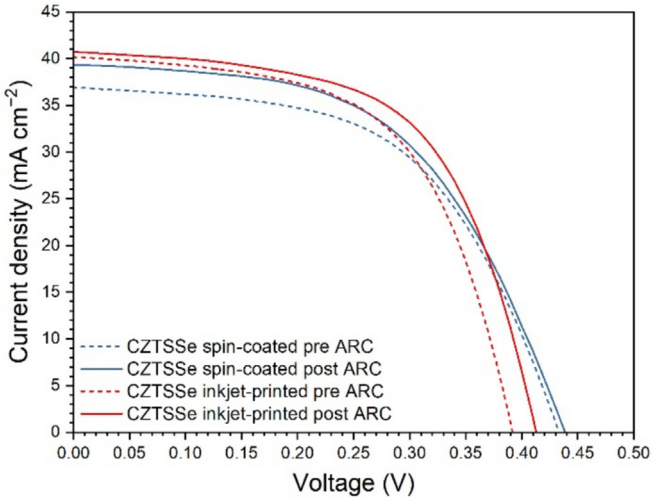

Fig. 5. *J-V* curves under illumination (1 sun, AM 1.5G, pre- and post-ARC) of spin-coated (blue) and inkjet-printed (red) SOL-B CZTSSe champion solar cells.

For the aforementioned champion solar devices, given the partial shading by Al contacts and the manual spot positioning, the Normalized External Quantum Efficiency (EQE) has been only qualitatively evaluated (Fig. 6). In both cases, the curves show a maximum around 550 nm, as expected from the literature [40]. More specifically, the normalized EQE spectra (Fig. 6a) reveal that the inkjet-printed devices show a better response compared to our spin-coated ones across almost the entire wavelength range. Charge extraction from CdS is improved, as indicated by the increment in the region between 350 and 550 nm [41]. The spectral range of 550 and 750 nm, on the other hand, suggests that there is room for improvement regarding the p-n junction interface; further work should focus on engineering this interface to fulfil the remaining V_{OC} gap [41,42]. The inkjet-produced CZTSSe demonstrated more uniform photon charge conversion in the bulk, as indicated by the EQE trend in the 750–1050 nm range [41]. Indeed, the most pronounced enhancement occurs in the 850–1450 nm region. The inkjet-printed device exhibits a more extended near-infrared tail, consistent with the improved material quality, which contributes to a superior near-infrared response. The band gap is slightly narrower: 1.02 eV for the inkjet device vs. 1.07 eV for the spin-coated one (Fig. 6b).

To further investigate the photovoltaic behavior of CZTSSe devices prepared with spin coating and inkjet printing techniques, both types of solar cells have been modeled through SCAPS-1D software to derive R_S (series resistance) and R_{SH} (shunt resistance)

Table 2
Solar cell parameters for the champion devices pre- and post-ARC produced with SOL-B, both by spin-coating and inkjet-printing.

Device	ARC	PV parameters			
		J_{SC} (mA cm^{-2})	V_{OC} (mV)	*FF* (%)	η (%)
CZTSSe	No	36.8	436	57.1	9.17
spin-coated	Yes	39.9	441	54.5	9.59
CZTSSe	No	40.4	400	58.7	9.48
inkjet-printed	Yes	40.5	420	61.0	10.4

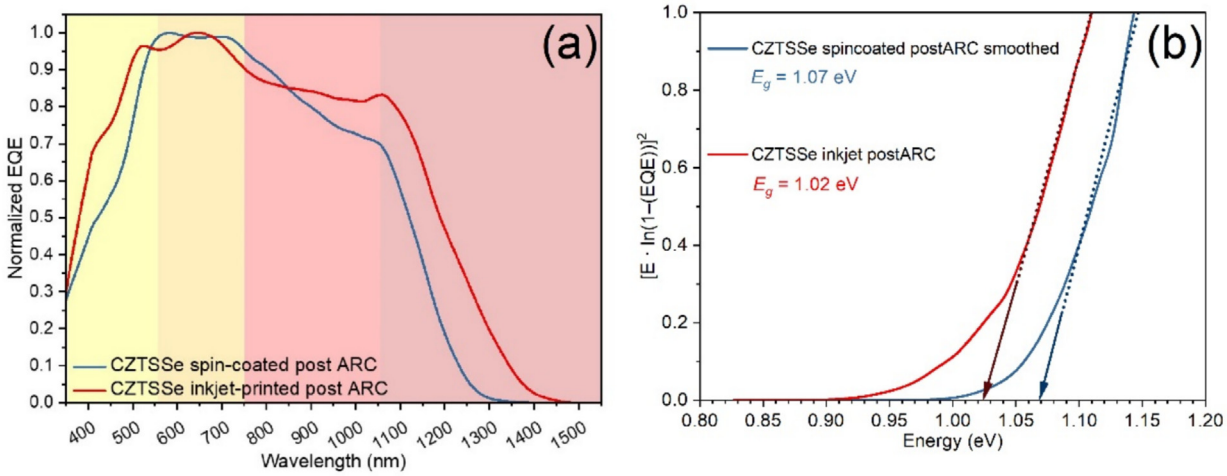

Fig. 6. (a) Normalized EQE curves of spin-coated (blue) and inkjet-printed (red) champion SOL-B CZTSSe solar cells, with the anti-reflecting coating (ARC); (b) Plot of [*h*ν ln (1 − EQE)]^2 against hν near band edge for band gap estimation (spin-coated: fitting R^2 = 0.96635; inkjet-printed: fitting R^2 = 0.99241).

values. All the parameters for the simulation were selected from the literature and refined to fit experimental data [43–46], while the E_g value used was derived from the EQE spectra. The doping density, directly related to copper vacancies (V_{Cu}), was set in the order of 10^{16} cm^{-3}, based on the copper content in the material [47] and considering the effect of Li-doping [27,48]. Fig. 7 shows the comparison between simulated and experimental *J-V* curves for spin-coated devices (Fig. 7a–c) and inkjet-printed ones (Fig. 7d–f). In the samples prepared employing SOL-A, R_{SH} for the inkjet-printed sample is 1.0×10^3 Ω cm^2, which is significantly higher than the spin-coated one, which is 4.5×10^1 Ω cm^2, indicating a reduction in current leakage; a slight reduction in R_S, which is beneficial for the device performance, is also found ($R_{S\ inkjet}$ = 6.2×10^{-1} Ω cm^2 vs. $R_{S\ spin\_coat}$ = 7.2×10^{-1} Ω cm^2). These differences in resistance values explain the *FF* increase, from 43.7% to 55.3%, moving from spin-coating to inkjet CZTSSe deposition. In fact, the inkjet printing ensures a much more compact surface of the thin film, thereby reducing alternative pathways for current leakage and avoiding shunts in the device, as proved through SEM top-view imaging (Fig. 8). When SOL-B is employed, the improved morphology of the kesterite layer prepared with both techniques results in very high and comparable shunt resistance values ($R_{SH\ inkjet}$ = 2.0×10^3 Ω cm^2 vs. $R_{SH\ spin\text{-}coat}$ = 2.4×10^3 Ω cm^2); this remarkable increase in R_{SH} values for the samples prepared with the SOL-B can be ascribed to the formation of a very compact CZTSSe layer with a bigger average grain size. The higher *FF%* value obtained with inkjet deposition (FF_{inkjet} = 58.7% vs. $FF_{spin\text{-}coat}$ = 57.1%) is explained by the strong difference in series resistance values ($R_{S\ inkjet}$ = 4.7×10^{-1} Ω cm^2 vs. $R_{S\ spin\text{-}coat}$ = 1.64 Ω cm^2). The application of ARC on the samples prepared with the two different techniques induces a slight increase in series resistance ($R_{S\ inkjet\ post\ ARC}$ = 5.9×10^{-1} Ω cm^2 vs. $R_{S\ spin\text{-}coat}$ = 2.0 Ω cm^2). This effect is counterbalanced by the increase of shunt resistance in the inkjet-printed sample post ARC (R_{SH} = 3.0×10^3 Ω cm^2), resulting in a *FF* enhancement (FF_{inkjet} from 58.7% to 61.0%), while a slight decrease of the shunt resistance in the spin-coated sample ($R_{SH\ spin\text{-}coat}$ = 1.8×10^3 Ω cm^2) leads to the *FF* reduction (54.7%) after ARC deposition. The ARC deposition process could be further optimized to enhance even more its beneficial effect by avoiding the above-mentioned slight R_S increase, which is also responsible for the modest gain in J_{SC}.

It follows that the morphology of the thin films was investigated by SEM imaging to evaluate the homogeneity and compactness of the absorber materials, eventually highlighting morphological differences between the two deposition methods and thereby explaining the different solar cell behaviors. The SOL-A inkjet-printed thin films (Fig. 8d–f) surfaces are quite compact and homogeneous, especially if compared to the SOL-A spin-coated ones (Fig. 8a–c), where holes and cavities are clearly visible. These results indicate that the controlled droplet deposition in inkjet printing promoted a better material self-organization, leading to more uniform and compact CZTSSe films. On the contrary, spin coating resulted in less uniform nucleation and in the formation of separated grains and voids, which can act as shunt pathways, consistent with the lower *FF* observed [49]. Inkjet printing enhances the crystallization of CZTSSe films through a combination of controlled material delivery and more favorable intermediate steps during drying and pyrolysis. Unlike spin coating, where rapid solvent removal often leads to compositional inhomogeneities, uneven film thickness, and premature nucleation, this technology deposits the precursor in precisely metered droplets that promote a uniform spatial distribution of the solutes. This controlled deposition allows the wet film to reorganize more homogeneously during drying, leading to denser precursor layers with fewer shrinkage induced voids. As a result, nucleation during the initial stages of crystallization proceeds more uniformly, which in turn

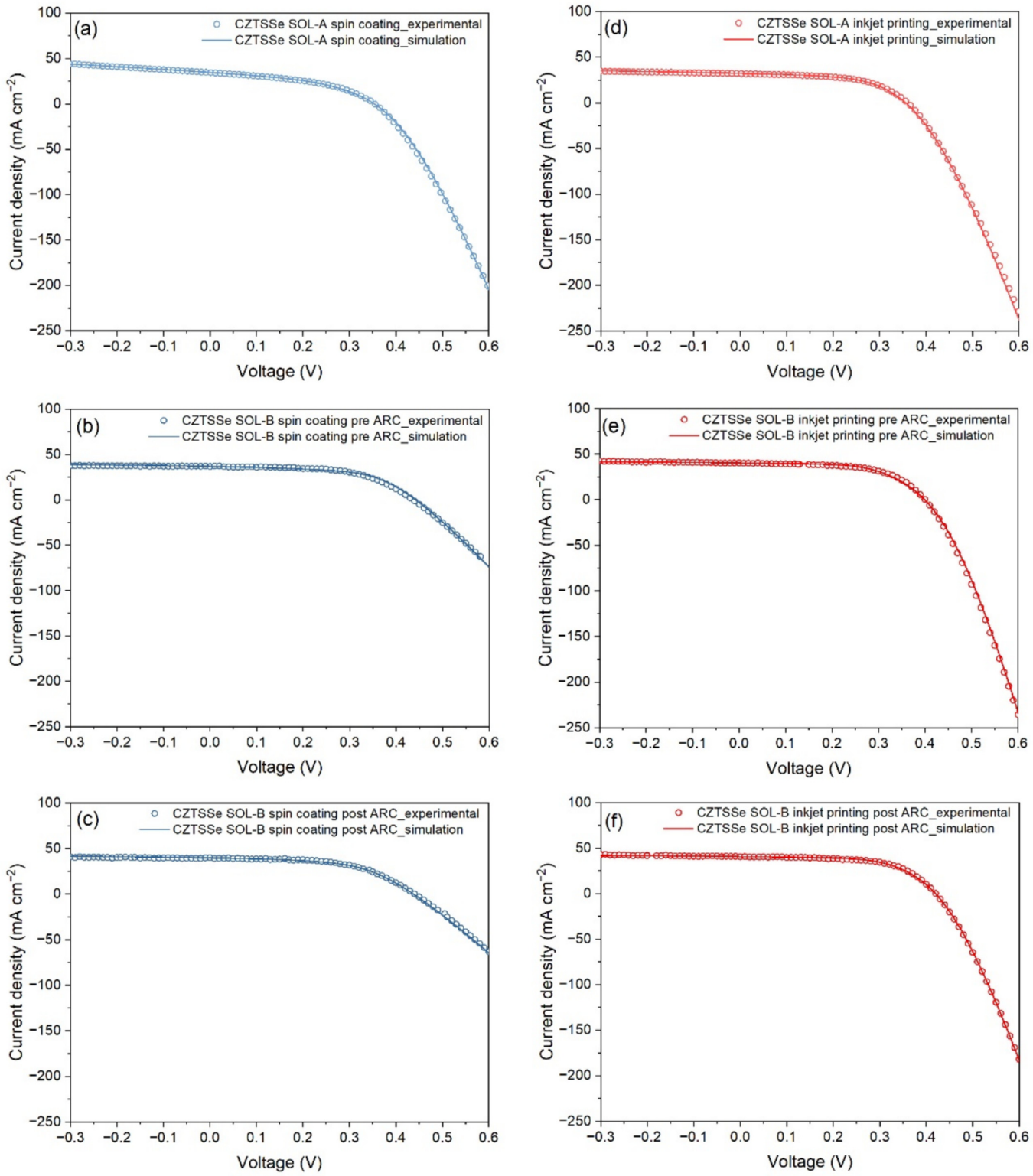

Fig. 7. SCAPS-1D fitting and simulation of the champion *J-V* curves. Comparison between simulated (continuous line) and experimental (dots) *J-V* curves for spin-coated SOL-A (a), spin-coated SOL-B pre-ARC (b), spin-coated SOL-B post-ARC (c), inkjet-printed SOL-A (d), inkjet-printed SOL-B pre-ARC (e), and inkjet-printed SOL-B post-ARC (f).

facilitates more effective lateral and vertical grain coalescence during high temperature annealing [30]. A further advantage of the inkjet printing deposition technique comes from the possibility to a specifically designed pattern. In this case, a cross hatched serpentine printing pattern was chosen to ensure uniform coverage of the available area. This strategy minimizes the risk of local material depletion during droplet deposition, effectively suppressing the formation of uncoated regions, holes, and cavities. Overall, the combined effects of uniform precursor distribution, enhanced densification, and controlled solvent evaporation make the printing/drying/pyrolysis pathway intrinsically more favorable for homogeneous nucleation and improved grain growth. However,

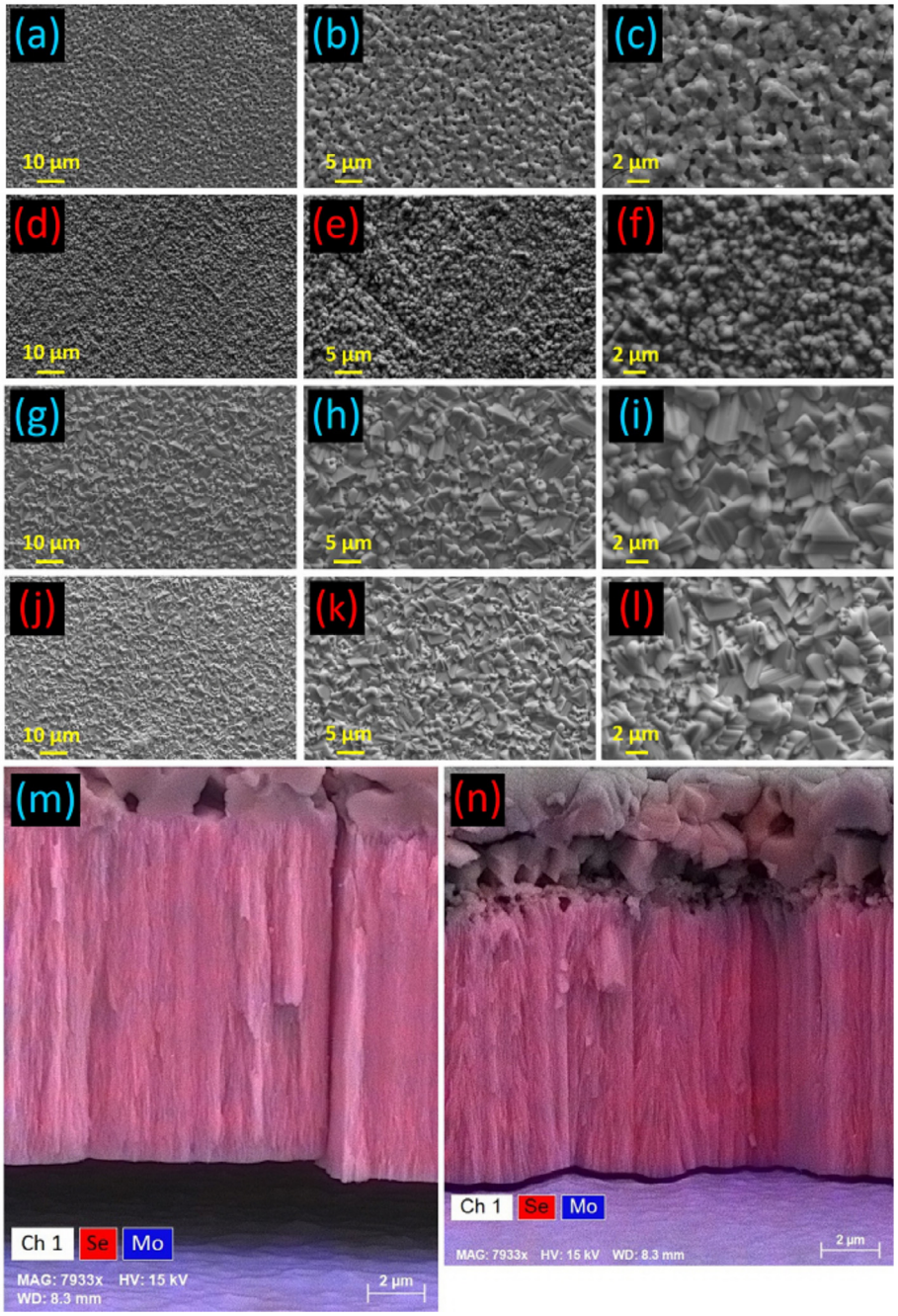

Fig. 8. SEM planar images of SOL-A spin-coated CZTSSe samples at 5 kX, 10 kX, and 20 kX magnification, respectively (a–c); SEM planar images of SOL-A inkjet-printed samples at 5 kX, 10 kX, and 20 kX magnification, respectively (d–f); SEM planar images of SOL-B spin-coated CZTSSe samples at 5 kX, 10 kX, and 20 kX magnification, respectively (g–i); SEM planar images of SOL-B inkjet-printed samples at 5 kX, 10 kX, and 20 kX magnification, respectively (j–l); SEM-EDS cross-section of the $MoSe_2$ layer as a result of the selenization process on the Mo foil back contact in our spin-coated (m) and inkjet-printed (n) devices.

despite the compact surface achieved with SOL-A combined with inkjet deposition, it did not guarantee a sensible increase in grain dimension, thus leaving open possible charge recombination at the grain boundaries, possibly being the main reason for lower efficiencies when SOL-A was employed. The lower surface tension of SOL-B suggests more homogeneous nucleation, with larger, more uniform grains and a reduction in holes and defects. Moreover, the higher concentration of SOL-B leads to denser wet films, which allows for better coverage of the holes and more homogeneous layers. Indeed, a greater local availability of precursors favors the coalescence and growth of the grains. In fact, SOL-B leads to the formation of large dimension grains and to a more compact surface already with spin-coating (Fig. 8g–i) and even more pronounced with inkjet-printing (Fig. 8j–l). In particular, SOL-B spin-coated samples still display occasional cavities, which are completely absent from those produced by inkjet printing, again demonstrating how the latter not only is an industrially appealing deposition system but also leads to higher quality materials.

To further verify what was observed by XRD patterns (Fig. 1), SEM-EDS cross-section imaging was performed on both spin-coated and inkjet-printed samples (Fig. 8m, n). The images highlight a higher $MoSe_2$ thickness in our spin-coated samples rather than in the inkjet-printed ones, as predicted by the already reported XRD patterns in Fig. 1. As reported and well known, in

CZTSSe phase formation, the Se diffusion has a primary role in controlling the crystallization process. The results obtained suggest a more controlled crystallization process thanks to the inkjet printing deposition technique, leading to a more compact material. Considering these, both XRD and SEM analysis converge on the same conclusion.

Aiming to propose an industrially scalable and reliable process, as well as a suitable real-life product integration, the PV parameters of our SOL-B, both spin-coated and inkjet-printed flexible devices, have been recorded under multiple bending cycles (up to 500), over a cylinder of fixed bending radius of 0.75 cm. The protocol followed is the one that uses a rod of a specific radius according to which, if a film is wrapped tightly around the rod, the bending radius R will match the radius of the rod. In our case a cylinder with a fixed bending radius of 0.75 cm was used, the devices were bent outwards (convex) and measured to have the bending axis aligned parallel to the electron flow [22]. Bending cycles were manually performed by the operator. By analyzing the data reported in Fig. 9, it is evident how the inkjet-printed solar cells outmatch our spin-coated ones in all the categories and especially in η%, by retaining around 90% of the original efficiency over 500 bending cycles. Contrarily, our spin-coated PV cells retain less than 65% of their starting efficiency, mainly due to a non-negligible J_{SC} and *FF* loss during bending. As already evidenced by SEM imaging, SOL-B leads to a more homogeneous nucleation, with larger, more uniform grains and a reduction in holes and defects. Thanks to the higher concentration of SOL-B, denser wet films also allow for better adhesion to the substrate and better resistance to stress. Again, inkjet printing has been demonstrated not only to be an industrially appealing deposition technology but also to lead to stress-proof materials and therefore PV devices.

4. Conclusions

In this work, stable MOE-based inks have been used as precursors for inkjet printing in order to produce scalable and highly efficient, flexible CZTSSe thin-film PV devices. Inkjet printing easily produces compact and uniform thin films on flexible substrates, and in our case, it allowed to reach even higher efficiencies than our spin-coated reference devices. This sustainable and reliable deposition method eliminates precursor waste, significantly reduces processing time, and, above all, yields a higher-quality material, thereby enhancing both the photovoltaic parameters and the mechanical resilience of the films under bending. Thanks to the precursor solution and inkjet-printing parameters optimization, the first flexible and inkjet-printed CZTSSe solar devices have been produced, scoring a record efficiency of η = 10.4%, which aligns with the current state-of-the-art (Fig. 10). These very promising results highlight the feasibility of this process, thus paving new ways for the scale-up of flexible CZTSSe thin-film solar cells. Thanks to a drop-on-demand solution-based technique, such as inkjet printing, the industrial mass production of efficient, flex-

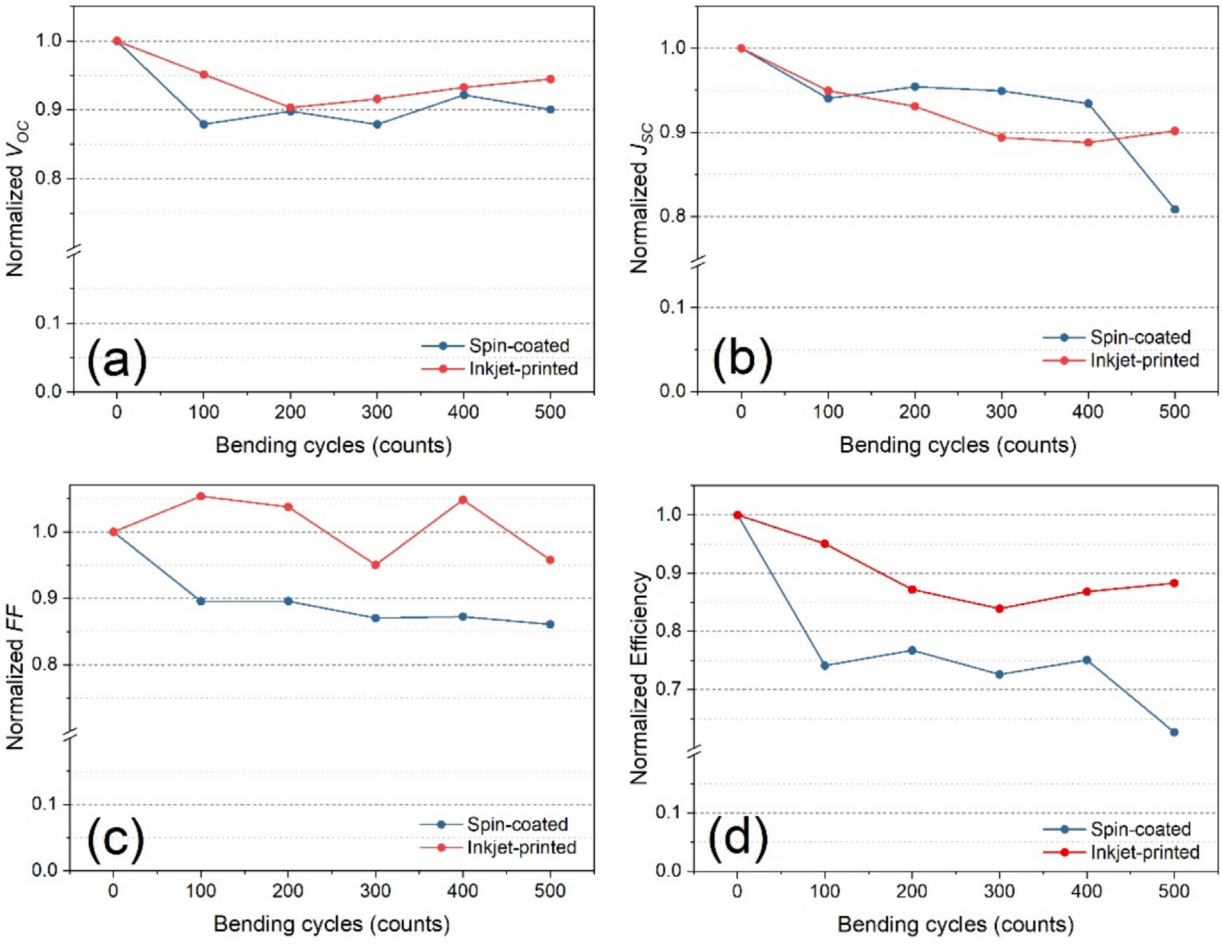

Fig. 9. Solar cell parameters V_{OC} (a), J_{SC} (b), *FF* (c), and η (d), for SOL-B spin-coated (blue) and inkjet-printed (red) devices in a range from 100 to 500 bending cycles, over a cylinder with a fixed bending radius of 0.75 cm.

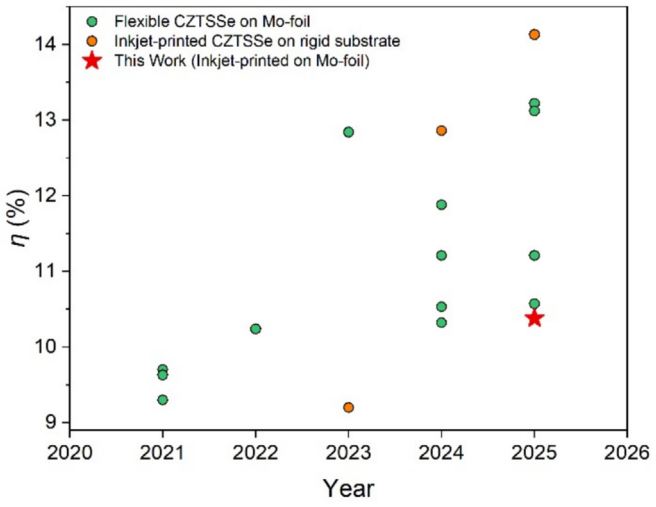

Fig. 10. State-of-the-art of the record efficiencies of solution-processed kesterite solar cells on flexible Mo-foil (green dots) [11–22,24,27,50], and of inkjet-printed on rigid substrates (orange dots) [23,31,32]. The record of this work, being the first to combine flexible substrates with inkjet printing, is highlighted with a red star.

ible CZTSSe PV devices is finally possible, helping to fulfill the needs of integrated PV application areas.

Data availability

The authors declare that all data supporting this study are available in the main manuscript.

CRediT authorship contribution statement

Berenice Elena Gaia Colombo: Writing – review & editing, Validation, Methodology, Investigation, Formal analysis, Data curation. **Alex Sangiorgi:** Writing – review & editing, Writing – original draft, Validation, Project administration, Methodology, Investigation, Formal analysis, Data curation, Conceptualization. **Giorgio Tseberlidis:** Writing – review & editing, Writing – original draft, Supervision, Project administration, Methodology, Investigation, Formal analysis, Data curation, Conceptualization. **Carla Gobbo:** Writing – review & editing, Validation, Methodology, Data curation. **Fabio Butrichi:** Writing – review & editing, Writing – original draft, Visualization, Validation, Formal analysis, Data curation. **Vanira Trifiletti:** Writing – review & editing, Writing – original draft, Visualization, Validation, Formal analysis, Data curation. **Maurizio Acciarri:** Supervision, Formal analysis, Data curation. **Alessandra Sanson:** Supervision, Resources, Project administration, Funding acquisition. **Simona Binetti:** Writing – review & editing, Supervision, Resources, Project administration, Funding acquisition.

Declaration of competing interest

The authors declare that they have no known competing financial interests or personal relationships that could have appeared to influence the work reported in this paper.

Acknowledgements

This study is a result of the research project "nuovi Concetti, mAteriali e tecnologie per l'iNtegrazione del fotoVoltAico negli edifici in uno scenario di generazione diffuSa" [CANVAS], funded by the Italian Ministry of the Environment and the Energy Security, through the Research Fund for the Italian Electrical System (type-A call, published on G.U.R.I. n. 192 on 18-08-2022). This work was also supported by the "MUSA—Multilayered Urban Sustainability Action" project (Project Code ECS 000037), funded by the European Union, via NextGenerationEU, under the National Recovery and Resilience Plan (NRRP) Mission 4 Component 2 Investment Line 1.5: Strengthening of research structures and creation of R&D "innovation ecosystems", set up of "territorial leaders in R&D". The author F.B. acknowledges the Dottorato di Interesse Nazionale "Photovoltaics". The authors thank Prof. Giancarlo Capitani and the Piattaforma di Microscopia di Milano-Bicocca for the precious contribution in cross-section SEM-EDS imaging.

References

[1] K. Ito, Copper Zinc Tin Sulfide-Based Thin-Film Solar Cells, Wiley Books, Hoboken, 2015.
[2] G. Tseberlidis, C. Gobbo, V. Trifiletti, V. Di Palma, S. Binetti, Sustain. Mater. Technol. 41 (2024) e01003.
[3] C. Platzer-Björkman, N. Barreau, M. Bär, L. Choubrac, L. Grenet, J. Heo, T. Kubart, A. Mittiga, Y. Sanchez, J. Scragg, S. Sinha, M. Valentini, J. Phys. Energy 1 (2019) 044005.
[4] K. Jagadish, G.K. Rahane, B.S. Kumar, D.R. Borkar, K. Chordiya, S.R. Kavanagh, A. Roy, T. Debnath, S. Kolekar, M.U. Kahaly, S.S. Mali, S. Pal, N. Gasparini, D.P. Dubal, S.R. Rondiya, Small 20 (2024) 2402048.
[5] A. Le Donne, V. Trifiletti, S. Binetti, Front. Chem. 7 (2019) 297.
[6] R. Herrero, L. Olivieri, M. Victoria, R. Núñez, in: Fundamentals of Solar Cells and Photovoltaic Systems Engineering, Academic Press, New York, 2025, pp. 365–400.
[7] N. Martín-Chivelet, K. Kapsis, H.R. Wilson, V. Delisle, R. Yang, L. Olivieri, J. Polo, J. Eisenlohr, B. Roy, L. Maturi, G. Otnes, M. Dallapiccola, W.M.P. Upalakshi Wijeratne, Energy Build. 262 (2022) 111998.
[8] D.R. Sajitha, B. Stephen, A. Nakamura, M. Selvaraj, S.T. Salammal, S. Hussain, Prog. Solid State Chem. 76 (2024) 100490.
[9] H. Katagiri, N. Sasaguchi, S. Hando, S. Hoshino, J. Ohashi, T. Yokota, Sol. Energy Mater. Sol. Cells 49 (1997) 407–414.
[10] M.A. Green, E.D. Dunlop, M. Yoshita, N. Kopidakis, K. Bothe, G. Siefer, X. Hao, J. Y. Jiang, Prog. Photovoltaics Res. Appl. 33 (2025) 795–810.
[11] H. Xu, R. Meng, X. Xu, L. Wu, Y. Sun, Y. Liu, Z. Wang, N. Wang, M. Li, Y. Zhang, Small Methods 9 (2025) 2401084.
[12] H. Xu, R. Meng, X. Xu, Y. Liu, Y. Sun, Y. Zhang, Small 20 (2024) 2408122.
[13] L. Lou, J. Wang, Y. Li, K. Yin, X. Xu, B. Zhang, M. Jiao, S. Chen, T. Guo, J. Wang, Y. Li, J. Shi, H. Wu, R. Xiao, H. Xin, Y. Luo, D. Li, Q. Meng, Joule 9 (2025) 102091.
[14] X. Xu, J. Zhou, K. Yin, J. Wang, L. Lou, D. Li, J. Shi, H. Wu, Y. Luo, Q. Meng, Adv. Energy Mater. 13 (2023) 2301701.
[15] Z. Su, W. Xie, Q. Sun, Y. Li, Z. Zhong, W. Wang, C. Zhang, H. Deng, S. Cheng, ACS Mater. Lett. 7 (2025) 1329–1335.
[16] Q. Sun, C. Shi, W. Xie, Y. Li, C. Zhang, J. Wu, Q. Zheng, H. Deng, S. Cheng, Adv. Sci. 11 (2024) 2306740.
[17] W. Xie, Q. Sun, Q. Yan, J. Wu, C. Zhang, Q. Zheng, Y. Lai, H. Deng, S. Cheng, Small 18 (2022) 2201347.
[18] Q. Sun, H. Deng, Q. Yan, B. Lin, W. Xie, J. Tang, C. Zhang, Q. Zheng, J. Wu, J. Yu, S. Cheng, ACS Appl. Energy Mater. 4 (2021) 14467–14475.
[19] H. Deng, Q. Sun, Z. Yang, W. Li, Q. Yan, C. Zhang, Q. Zheng, X. Wang, Y. Lai, S. Cheng, Nat. Commun. 12 (2021) 3107.
[20] H. Xu, N. Wang, R. Meng, X. Xu, Y. Liu, Q. Gao, J. Dong, J. Li, M. Li, L. Wu, Y. Zhang, ACS Energy Lett. 10 (2025) 4644–4654.
[21] J. Li, K. Sun, X. Yuan, J. Huang, M.A. Green, X. Hao, Npj Flex. Electron. 7 (2023) 16.
[22] C. Gobbo, Y. Gong, A. Jimenez-Arguijo, G. Tseberlidis, V. Trifiletti, C. Malerba, M. Valentini, P. Estarlich, E. Armelin, S. Lanzalaco, R. Po, S. Binetti, E. Saucedo, J. Mater. Chem. A 13 (2025) 25498–25508.
[23] Y. Mao, M. Wang, Y. Huang, Y. Deng, W. Chan, Z. Ren, E. Gu, S. Sangaraju, X. Lin, G. Yang, J. Energy Chem. 113 (2026) 872–880.
[24] Y. Zhang, Q. Sun, W. Xie, Y. Li, Z. Su, W. Xu, W. Wang, H. Deng, S. Cheng, J. Energy Chem. 105 (2025) 806–813.
[25] S. Deng, S. Wang, Y. Wang, Q. Xiao, Y. Meng, D. Kou, W. Zhou, Z. Zhou, Z. Zheng, S. Wu, J. Energy Chem. 95 (2024) 77–85.
[26] T. Enkhbat, E. Enkhbayar, N. Otgontamir, M.H. Sharif, M.S. Mina, S.Y. Kim, J. Kim, J. Energy Chem. 77 (2023) 239–246.
[27] Q. Yan, Q. Sun, H. Deng, W. Xie, C. Zhang, J. Wu, Q. Zheng, S. Cheng, J. Energy Chem. 75 (2022) 8–15.
[28] N. Sahu, B. Parija, S. Panigrahi, Indian J. Phys. 83 (2009) 493–502.
[29] J. Yus, Z. Gonzalez, A.J. Sanchez-Herencia, A. Sangiorgi, A. Sanson, C. Galassi, B. Ferrari, Open Ceram. 8 (2021) 100197.
[30] X. Lin, J. Kavalakkatt, M.Ch. Lux-Steiner, A. Ennaoui, Adv. Sci. 2 (2015) 1500028.
[31] S. Ge, H. Xu, T. Wang, E. Gu, X. Lin, G. Yang, ACS Mater. Lett. 5 (2023) 1767–1771.
[32] Y. Mao, T. Wang, Y. Jian, Y. Huang, Y. Deng, E. Gu, X. Lin, G. Yang, Adv. Funct. Mater. 35 (2025) 2416689.

[33] Y. Gong, A. Jimenez-Arguijo, A.G. Medaille, S. Moser, A. Basak, R. Scaffidi, R. Carron, D. Flandre, B. Vermang, S. Giraldo, H. Xin, A. Perez-Rodriguez, E. Saucedo, Adv. Funct. Mater. 34 (2024) 2404669.
[34] S.F. Kamarudin, N.H. Abdul Aziz, H.W. Lee, M. Jaafar, S. Sulaiman, Adv. Mater. Technol. 9 (2024) 2301875.
[35] M. Burgelman, P. Nollet, S. Degrave, Thin Solid Films 361–362 (2000) 527–532.
[36] Y. Gong, A. Jimenez-Arguijo, I. Caño, R. Scaffidi, C. Malerba, M. Valentini, D. Payno, A. Navarro-Güell, O. Segura-Blanch, D. Flandre, B. Vermang, A. Perez-Rodriguez, S. Giraldo, M. Placidi, Z. Jehl Li-Kao, E. Saucedo, Sol. RRL 9 (2025) 2400756.
[37] F. Butrichi, V. Trifiletti, G. Tseberlidis, B.E.G. Colombo, F. Taglietti, M. Rancan, L. Armelao, S. Binetti, Sol. Energy Mater. Sol. Cells 272 (2024) 112924.
[38] A. Wang, M. He, M.A. Green, K. Sun, X. Hao, Adv. Energy Mater. 13 (2023) 2203046.
[39] M. Dimitrievska, H. Xie, A. Fairbrother, X. Fontané, G. Gurieva, E. Saucedo, A. Pérez-Rodríguez, S. Schorr, V. Izquierdo-Roca, Appl. Phys. Lett. 105 (2014) 031913.
[40] A. Nakane, H. Tampo, M. Tamakoshi, S. Fujimoto, K.M. Kim, S. Kim, H. Shibata, S. Niki, H. Fujiwara, J. Appl. Phys. 120 (2016) 064505.
[41] H. Fujiwara, A. Nakane, D. Murata, H. Tampo, T. Matsui, H. Shibata, in: Spectroscopic Ellipsometry for Photovoltaics: Volume 2: Applications and Optical Data of Solar Cell Materials, Springer International Publishing, Cham, 2018, pp. 29–82.
[42] Z. Wang, R. Meng, H. Guo, Y. Sun, Y. Liu, H. Zhang, Z. Cao, J. Dong, X. Xu, G. Liang, L. Lou, D. Li, Q. Meng, Y. Zhang, Small 19 (2023) 2300634.
[43] A. Cherouana, R. Labbani, Appl. Surf. Sci. 424 (2017) 251–255.
[44] Y. Putthisigamany, K.S. Rahman, M.M.I. Sapeli, N. Ahmad Ludin, M. AdibIbrahim, P. Chelvanathan, Energy Fuel 38 (2024) 11188–11203.
[45] H. Jalali, A.A. Orouji, I. Gharibshahian, Sol. Energy Mater. Sol. Cells 260 (2023) 112492.
[46] C. Gobbo, V. Di Palma, V. Trifiletti, C. Malerba, M. Valentini, I. Matacena, S. Daliento, S. Binetti, M. Acciarri, G. Tseberlidis, Energies 16 (2023) 4137.
[47] G. Ren, D. Zhuang, M. Zhao, Y. Wei, Y. Wu, X. Li, X. Lyu, C. Wang, L. Hu, J. Wei, Q. Gong, Vacuum 173 (2020) 109121.
[48] A. Cabas-Vidani, S.G. Haass, C. Andres, R. Caballero, R. Figi, C. Schreiner, J.A. Márquez, C. Hages, T. Unold, D. Bleiner, A.N. Tiwari, Y.E. Romanyuk, Adv. Energy Mater. 8 (2018) 1801191.
[49] A.C. Mendhe, in: Simple Chemical Methods for Thin Film Deposition: Synthesis and Applications, Singapore, Springer Nature Singapore, 2023, pp. 387–424.
[50] H. Xu, S. Ge, W. Yang, S.N. Khan, Y. Huang, Y. Mai, E. Gu, X. Lin, G. Yang, J. Mater. Chem. A 9 (2021) 25062–25072.